# Elastic Full Waveform Inversion of the Moere Vest data

*Gustavo Alves*

## ABSTRACT

The extension of full waveform inversion (FWI) into elastic models can potentially address the limitations of acoustic FWI due to amplitude versus offset effects. I present results of applying an elastic FWI workflow to ocean-bottom nodes data. I show the steps used to pre-process the data and create an initial elastic model for inversion. Then, I apply these inputs into the inversion workflow and show how elastic inversion without pre-conditioning can be dominated by artifacts. Finally, I apply weighting operators in both residual space and image space and present results for the inverted model with data in the range of 2 to 5 Hz.

## INTRODUCTION

Full Waveform Inversion (FWI) has become one of the most prolific research topics in seismic imaging in recent years. Although the fundamentals of FWI were proposed 30 years ago (Tarantola, 1987), computational demands limited its generalized adoption.

Elastic Full Waveform Inversion (EFWI) pushes even further the computational demands of the method. Even when considering 2D problems with the velocity-stress formulation, the number of wave fields to be computed increases fivefold compared to the acoustic case. Also, the number of model parameters in EFWI increases threefold when compared to acoustic FWI. Finally, numerical stability and dispersion in elastic modeling require finer spatial and time sampling, due to slower propagating shear waves.

In this work, I apply the methodology developed in Alves (2015) to 2D field data in an EFWI workflow. I describe the pre-processing steps applied to the data and detail the objective function, search direction and step-length criteria. The inversion workflow uses the generic non-linear solver library developed by Biondi and Barnier (2017).

The data provided to SEP by Seabed Geosolutions were recorded in the Moere Vest field, offshore Norway. It was acquired using four component ocean-bottom nodes (4C OBNs) in a 2D array. In this work, I use a subset of this data composed of 141 nodes spaced 250 meters apart, totaling a 35 km receiver line. There are 1145 shots in this data set, with 100 meters between each shot, totaling a 114.5 km shot

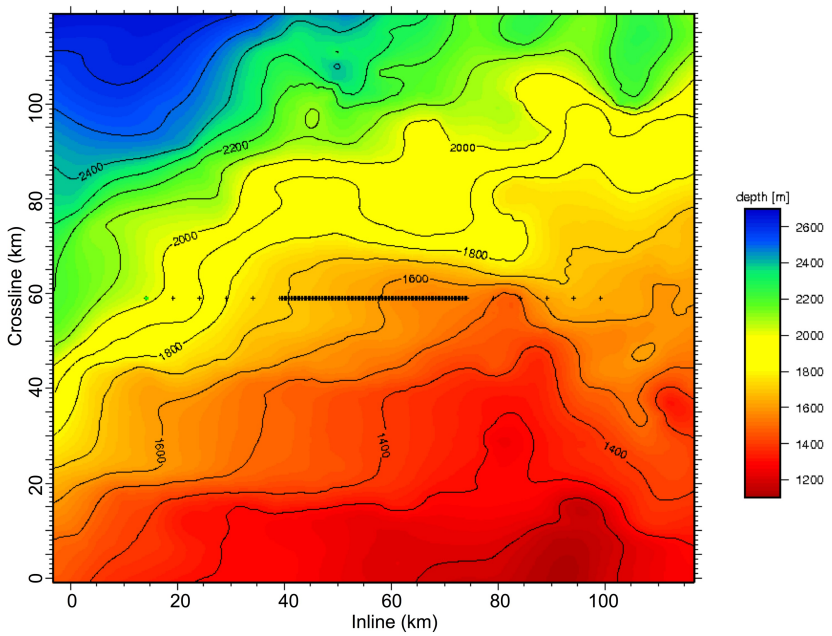


Figure 1: Bathimetry of the survey area and receiver positions. Receiver depths vary between 1942 m (West) to 1640 m (East). [**NR**]

line. The sail line overlaps the receiver line, which gives a maximum offset of 75 km. Figure 1 shows the bathymetry of the survey area and the locations of the receivers.

I perform EFWI with field data sorted in common-receiver gathers. To generate synthetic data in this domain, I apply reciprocity to find equivalent sources at node positions. Alves and Biondi (2017) describes how to obtain reciprocal data in the elastic case and its advantages.

## DATA PRE-PROCESSING

Before the data can be used for EFWI, it is important to pre-process it. By pre-processing, I mean the application of operators that remove features present in the field data but which are not modeled during the inversion. Since the EFWI process minimizes the $L_2$ norm of the data residual, it is paramount that field and synthetic data are as similar as possible. However, my goal is not to remove information related to the dynamics and kinematics of elastic events. Those should be unaffected by the pre-processing steps, so that they can be recovered by the EFWI.

Schematically, I can describe the pre-processing steps as the following chain of operators,

$$\mathbf{d_t} = \mathbf{F_{bub}F_{lc}S_{rec}Rd_{raw}}, \tag{1}$$

where $\mathbf{d_{raw}}$ is the original data, $\mathbf{R}$ is the rotation of horizontal geophones, $\mathbf{S_{rec}}$ is the receiver de-signature, $\mathbf{F_{lc}}$ is a low cut filter, $\mathbf{F_{bub}}$ is the bubble removal and $\mathbf{d_t}$ is the data prepared for EFWI.

## Data rotation

I start the pre-processing by rotating the horizontal components of the geophones. My goal is to separate data into radial and transverse. Since the shot line and receiver lines overlap, this is the same as having one horizontal component aligned with the acquisition and the other component orthogonal to it. To find the radial direction for each receiver, I apply an operator that rotates the horizontal components by 1 degree increments until I find the one that maximizes the energy of the first break in the radial component. Figure 2 shows data for horizontal geophones before and after rotation. I apply hyperbolic moveout (HMO) to the data and mark in red the areas above a fixed amplitude, to highlight the energy change. The rotation scheme applied here follows the methodology presented in Levin and Chang (2015).

## Receiver de-signature

Data recorded in the field is subject to the response of receivers used in the acquisition. This response includes, but is not limited to, coupling between receiver and elastic medium, frequency bandwidth and signature. I assume perfect coupling to the medium and combine all other effects as a convolution of wave field with receiver signature. I apply a de-convolution filter to the data by dividing it by the impulse response in the Fourier domain. A small stability term is added to avoid division by zero. Figure 3 shows the impulse responses of hydrophone and geophone receivers, as provided by Seabed.

## Bandpassing

I apply a low-cut filter at 2 Hz, aimed at removing swell noise. Figures 4a and 4b show the application of this frequency filter.

## De-bubble

The last step in the field data pre-processing is the removal of the air gun bubbles. The air guns used in marine acquisition generate pressure waves by injecting a fast

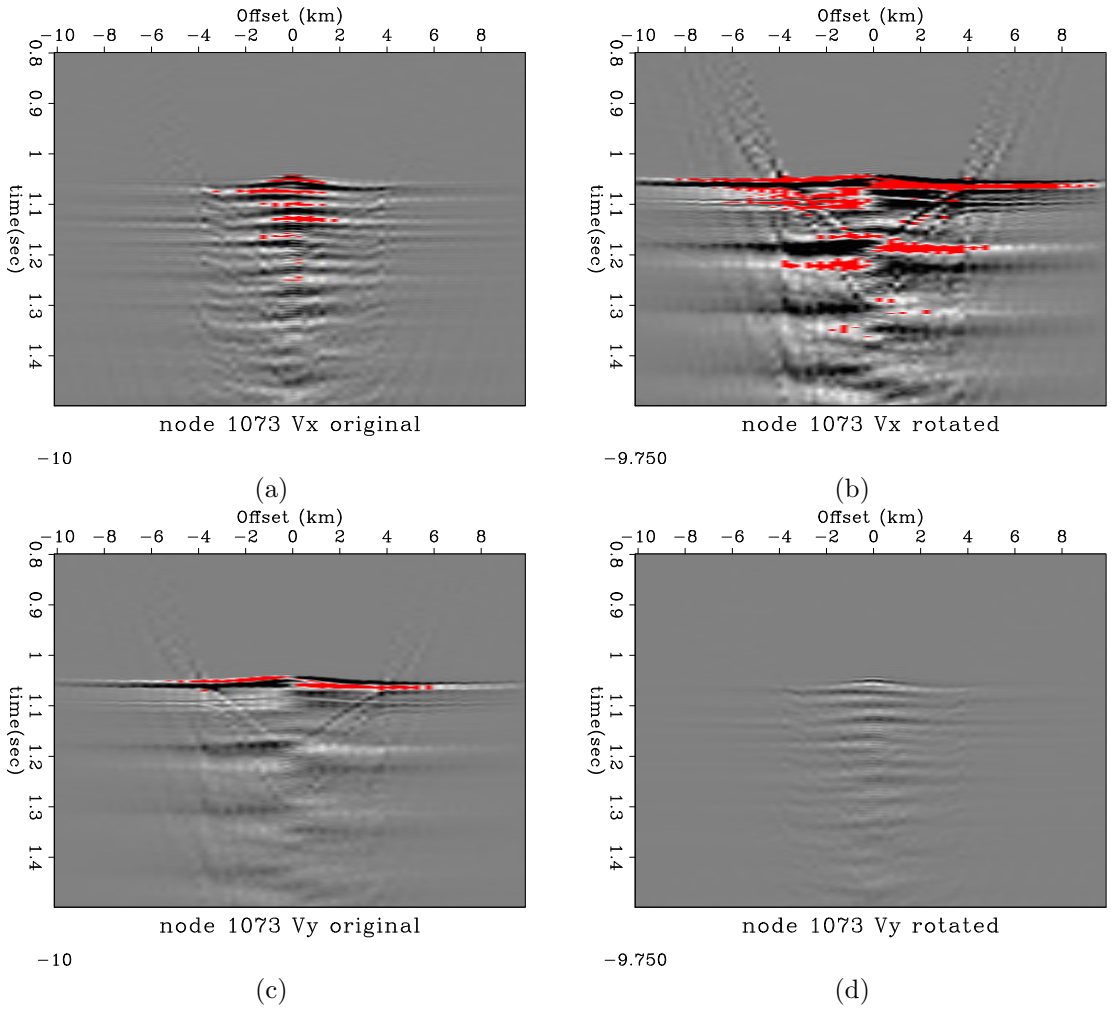


Figure 2: Common receiver gathers of the two horizontal geophones for a single node, before (a,c) and after (b,d) rotation. The red highlights indicate the amplitude above a clipping value. [**NR**]

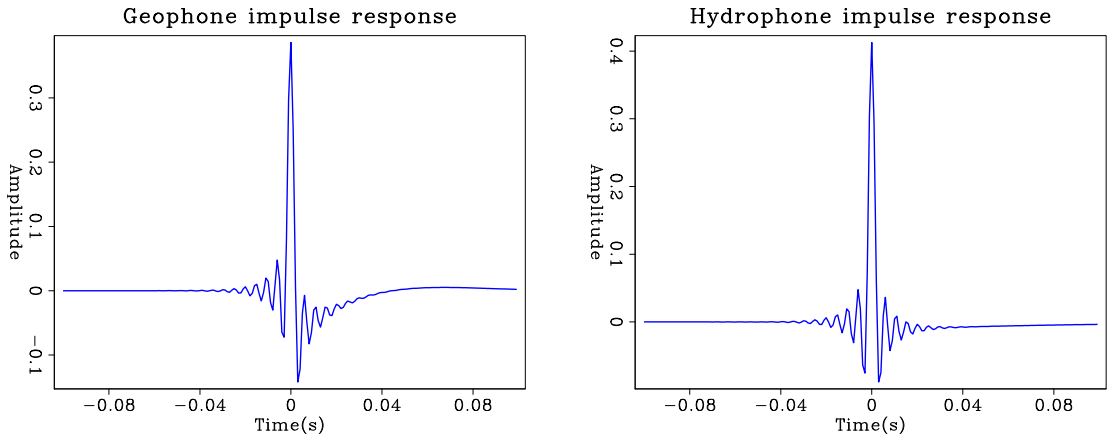


(a) (b)

Figure 3: Receiver impulse responses for the (a) geophones and (b) hydrophones used in the survey. [**NR**]

expanding air bubble in the water. This bubble oscillates as it surfaces and disperses, producing a periodic low frequency ringing in the data. While in theory this event could be introduced in the wavelet of the synthetic modeling, it would represent a novelty in traditional imaging with challenges of its own. Since the goal of this work is not to study this topic, I choose to remove the bubble effect.

I remove the bubbles by applying an autoregression filter, also called a prediction error filter (PEF). This is a suitable method for removing events such as multiples or, in my case, bubble effects, where the time and length of the events is predictable. For a detailed description of PEFs, I refer to Claerbout and Fomel (2008). Figures 4b and 4c shows data before and after de-bubble, respectively.

# DATA MODELING

While the pre-processing described in the previous section deals with the many undesired effects present in field data, the steps in this section are aimed at improving the generation of synthetic data.

## Source wavelet estimation

The objective function is essentially a measure of the difference between the observed data in the field and the data synthetically generated by the modeling. Therefore, it is very important to find a good estimate of the source wavelet, to minimize the residual between equivalent events in each data.

A very robust method to approximate the source wavelet is by performing a linear inversion of the direct arrivals in the field data. In the case of marine data, the

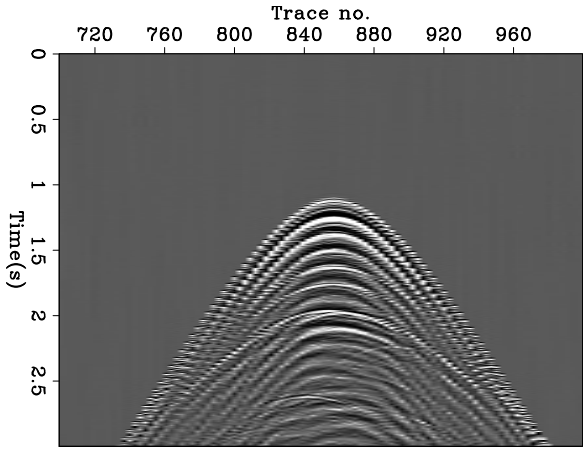


(a)

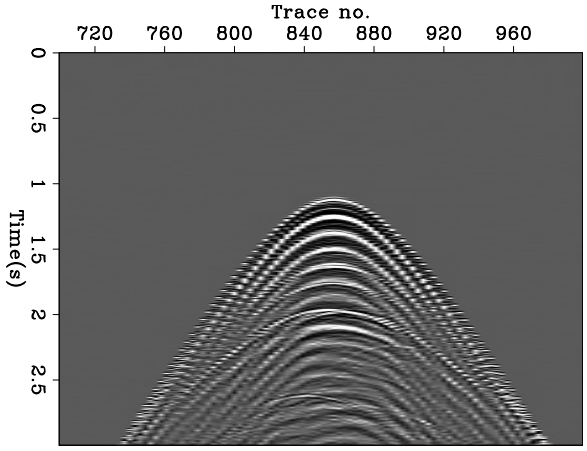


(b)

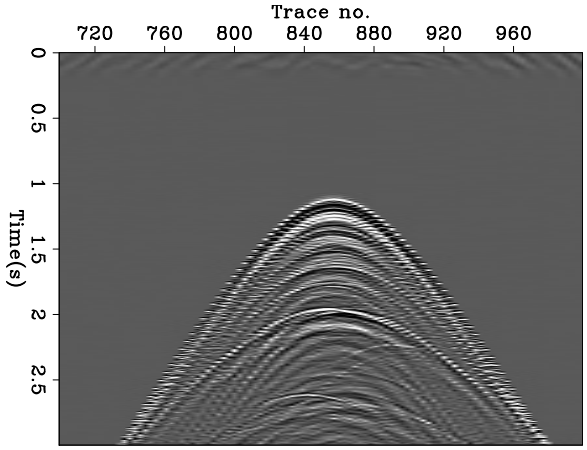


(c)

Figure 4: Vertical geophone data (a) before and (b) after band-passing and (c) after bubble removal by prediction error filtering. [**ER**]

direct arrivals travel only through an approximately constant medium (water), so the background model is known and the only parameter to be inverted for is the source wavelet itself.

Figure 5 shows the data residual of the direct arrival for one gather before and after wavelet estimation. The initial estimated source signature is zero, so the initial residuals are just the observed data, while the final residuals are obtained after 100 iterations. Figure 6 displays the objective function for this inversion and 7 shows the estimated wavelet.

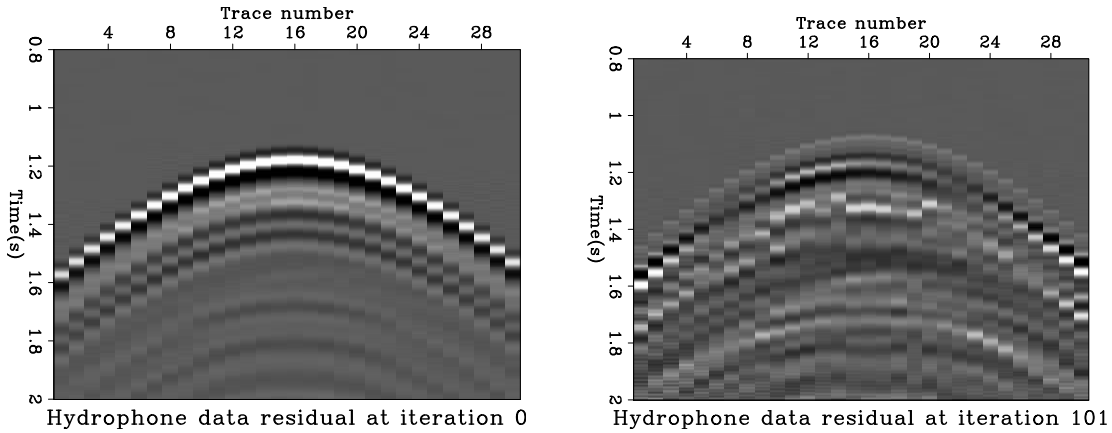


(a) (b)

Figure 5: Data residual (a) before and (b) after wavelet estimation. [**ER**]

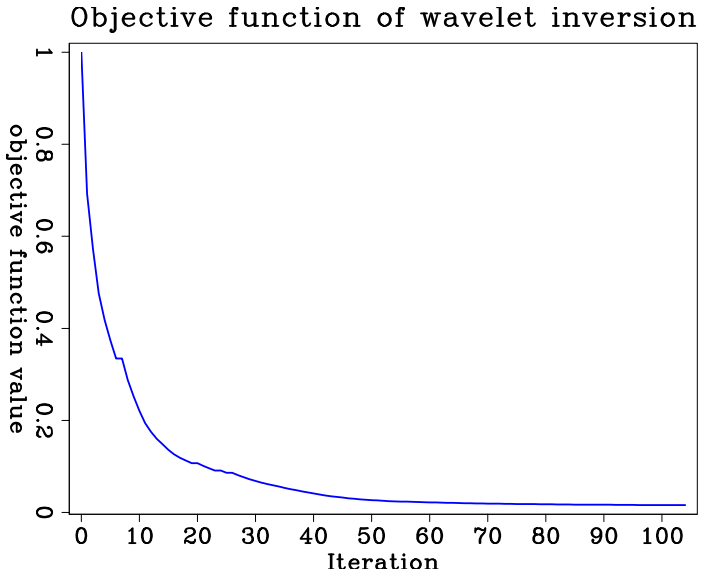


Figure 6: Objective function for the linear inversion of the source wavelet. [**ER**]

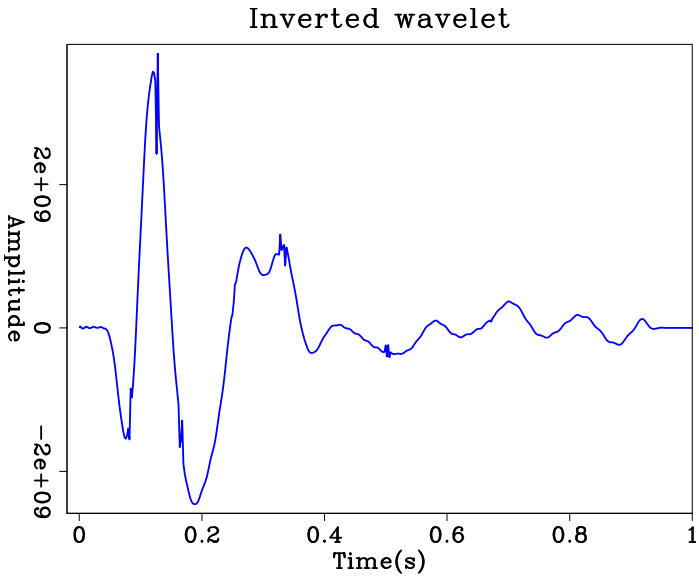


Figure 7: Final estimated source inverted from the direct arrivals in the field data. [**ER**]

## Data reciprocity

Both field and synthetic data used in the inversion are sorted in common-receiver gathers. To generate common-receiver gather synthetic data, I apply the elastic reciprocity theorem (Aki and Richards, 1980) to the hydrophone and geophone components. While the pressure (hydrophone) data is trivially obtained from acoustic reciprocity, vector data (geophones) need to be understood more carefully. I refer to Alves and Biondi (2017) for an in-depth analysis of this problem.

# INITIAL MODEL

The survey area is located in the Moere Basin, in the Norwegian-Greenland Sea. The Moere Basin is composed mainly of Lower Cretaceous to Late Oligocene shales, marine sandstone sequences during the Upper Cretaceous and Paleocene, and Early Eocene lavas, which are characteristic throughout most of the Voering and Moere Basins (Brekke et al., 1999).

## $V_p/V_s$ ratio

I obtain initial estimates for $V_p$ and $V_s$ from Linear Moveout (LMO) analyses of ocean bottom and top of basalt refractions. Estimated velocties are $V_p = 2300m/s$ and $V_s = 1340m/s$ for the overburden, which results in a $V_p/V_s$ ratio of 1.72. A detailed explanation of how these velocities were estimated and how P-to-S conversions were

used to botain $V_p/V_s$ can be found in Moronfoyer et al. (2016).

## Reverse time migration

I use the depths of the OBNs and velocities estimated previously to create a simple two-layer model (see figure 8). I apply Elastic Reverse Time Migration (ERTM) to the pre-processed data with a smoothed version of this model, as can be seen on figure 9. The ERTM code I use is essentially the solution of the adjoint Born operator for the elastic imaging condition, as I have described previously in Alves (2015).

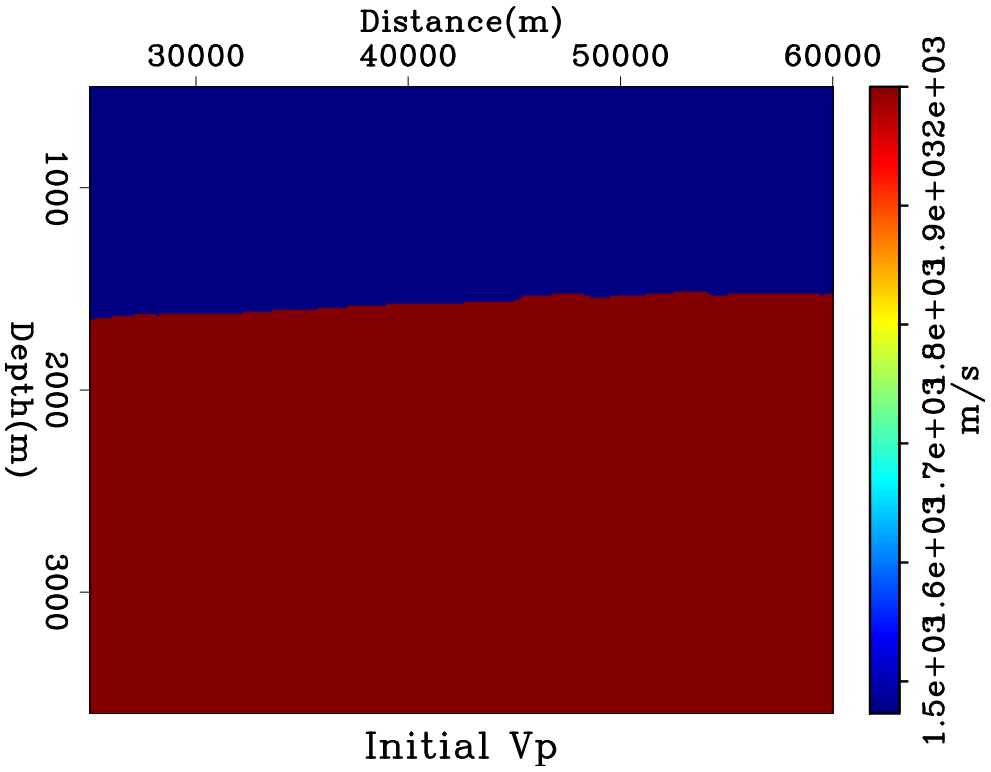


Figure 8: Initial $V_p$ velocity calculated from linear moveout anlysis and used for reverse time migration. Components $V_s$ and $\rho$ are not displayed for brevity. These look similar to $V_p$, respecting the estimated $V_p/V_s$ ratio and densities of $10^3 kg/m^3$ and $2.0 * 10^3 kg/m^3$ for water and overburden, respectively. [**ER**]

I use the ERTM image to manually pick the top and bottom of the basalt layer. While I expect that the basalt bottom will be pulled up in this image due to the lower velocities, it is enough to create an improved properties model for the EFWI workflow. Figure 10 shows the improved initial model.

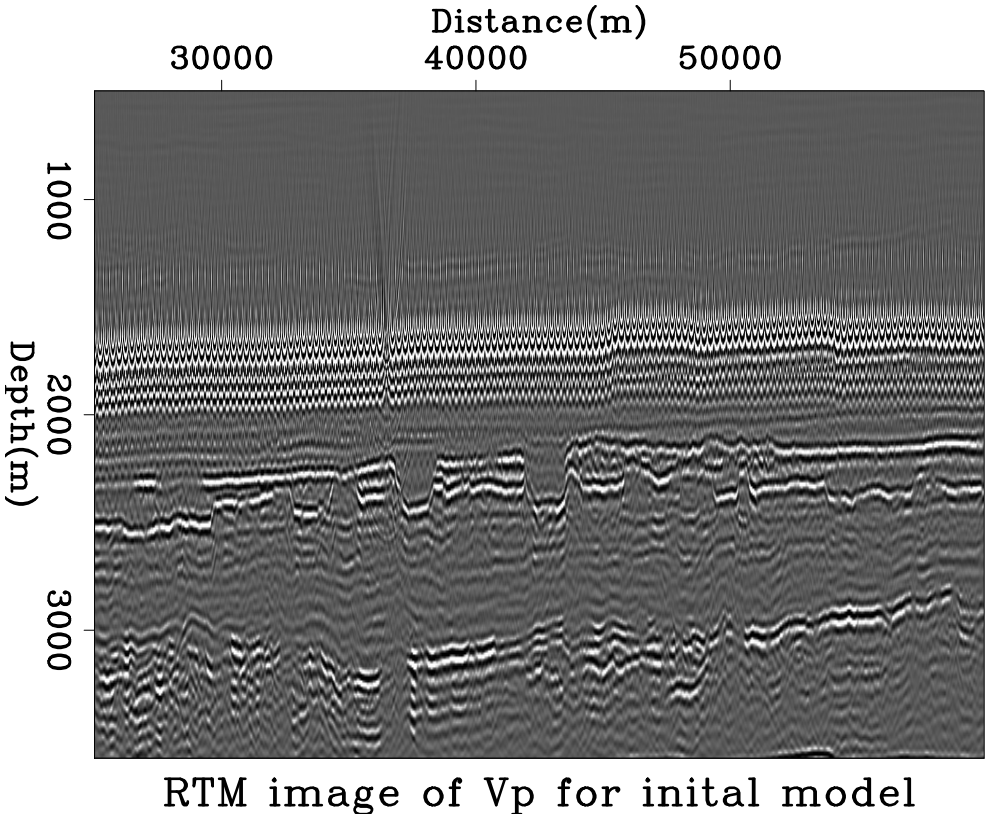


Figure 9: $V_p$ component of ERTM image using the initial properties model. Notice the acquisition footprint due to receiver density. [**CR**]

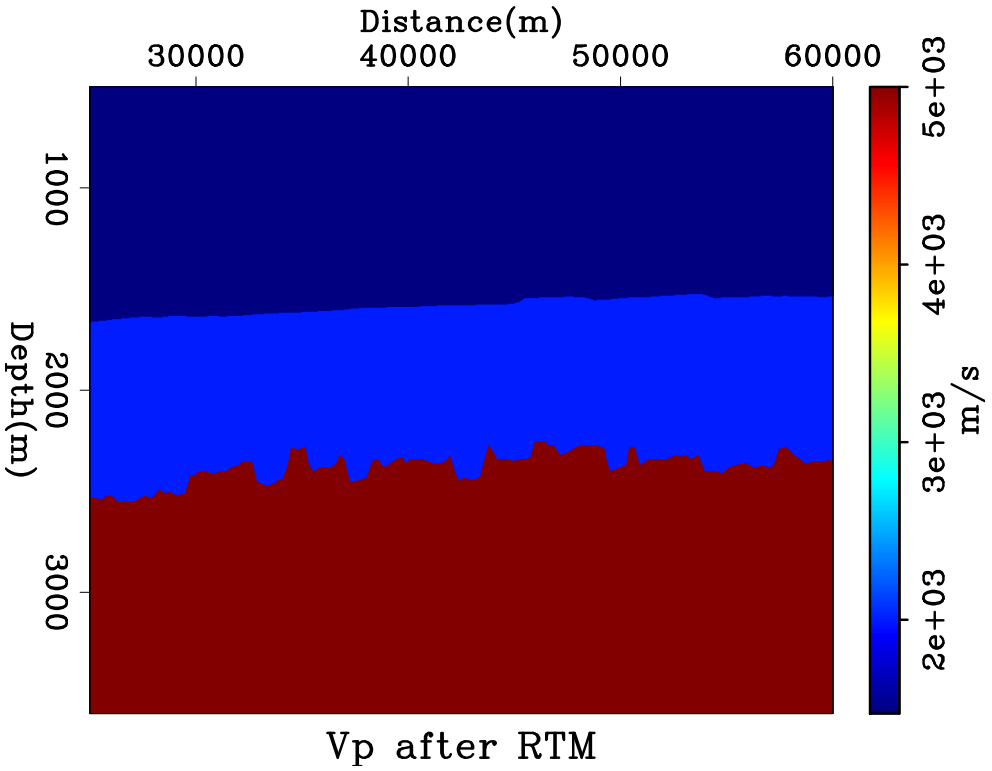


Figure 10: Improved initial velocity model with a basalt layer. [**NR**]

## ELASTIC FULL WAVEFORM INVERSION

There are many different forms of implementing a FWI workflow. Every step of the iteration process includes many choices, such as, type of Hessian approximation, norm of the objective function, search criteria for both direction and step length, use of pre conditioners and regularizers, etc. An interesting review on some of these choices can be found in Hager and Zhang (2006).

The objective function that I minimize is given by,

$$\phi(\mathbf{m}) = \frac{1}{2} \left\| \mathbf{W}(\mathbf{m}) - \mathbf{d_t} \right\|_2^2 , \tag{2}$$

where $\mathbf{W}(\mathbf{m})$ is the solution of the non-linear operator for model $\mathbf{m}$ and $\mathbf{d_t}$ is the field data. The gradient at iteration $n$, $\mathbf{g_n}$, used for the model update is,

$$\mathbf{g_n} = \left( \frac{\partial W(m)}{\partial m} \bigg|_{m_n} \right)^T , \tag{3}$$

where the partial derivative with respect to model parameters is the Jacobian of the function $\mathbf{W}(\mathbf{m})$, evaluated at the current background model, $\mathbf{m_n}$. The search direction is obtained by steepest-descent on the first iteration, followed by conjugate-gradient at every other iteration (Aster et al., 2005). The step length is obtained by parabolic search.

I run 20 iterations of EFWI. Data and synthetics are band-passed between 2 and 5 Hz, in order to focus the initial inversion in the long wavenumber updates of the properties model and decrease the chances of cycle skipping. Figure 11 shows an example of a gradient obtained for this implementation.

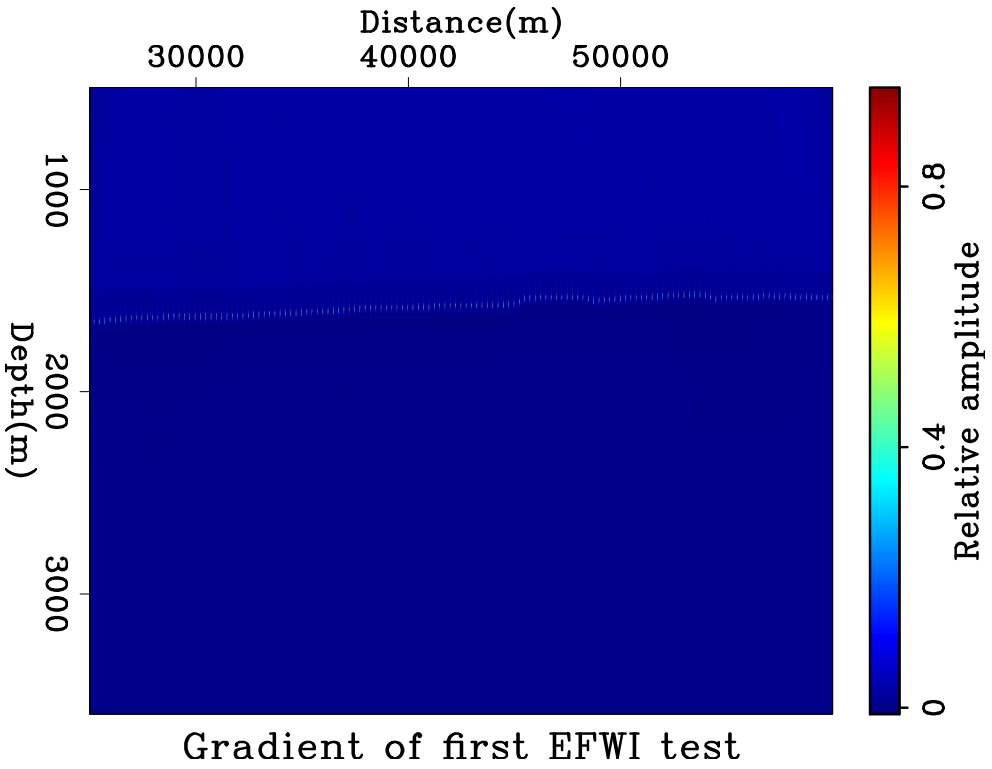


Figure 11: Example of gradient for first EFWI scheme without any data or gradient weighting. The gradient is dominated by updates at the nodes positions. [**CR**]

It is clear from figure 11 that the gradient only contains information at the node positions. Even after several iterations, the gradient remained similar and did not guide the inversion towards updates in the subsurface. Therefore, I improve on the previous objective function by adding a weighting term to the data residual,

$$\phi(\mathbf{m}) = \frac{1}{2} \left\| \mathbf{M_{res}}(\mathbf{W}(\mathbf{m}) - \mathbf{d_t}) \right\|_2^2 , \tag{4}$$

and also a weighting term to the gradient,

$$\tilde{\mathbf{g}}_\mathbf{n} = \mathbf{M_{grad}} \mathbf{g_n}, \tag{5}$$

where $\mathbf{M_{res}}$ is a weighting function applied to the data residual that dampens the direct arrivals and applies a gain proportional to $v_{rms}$ in time. $\mathbf{M_{grad}}$ is a weighting function to the gradient, that reduces the updates in the regions around the node positions.

After 20 iterations using this modified method and the same frequency range of 2-5Hz, it is possible to notice improvements in the sub-surface part of the model.

Figure 12 shows a comparison of the initial smoothed model and the improved inverted results. In this figure, a horizontal smoothing was applied to the final result to remove some of the footprint caused by the distance between nodes at the sea bottom.

## CONCLUSION

Pre-processing was done successfully with a combination of different filters and tools. I applied a deconvolution filter for receiver de-signature, a PEF to remove the air gun bubble, and a linear inversion to estimate the source wavelet.

The use of linear move-out information gave an initial estimate for the $V_p/V_s$ ratio. An initial RTM estimated the position for the top of the basalt layer with enough continuity to generate an improved model for inversion.

The use of a weighting operator was necessary to remove artifacts in the inversion. These artifacts were likely caused by discontinuities in the spatial first derivatives of the particle velocities at the nodes positions, although a more careful analysis of the problem would be required to confirm this hipotesis. It is important to recall that, because spatial reciprocity is being applied, the synthetic sources are positioned at the nodes coordinates.

The inverted properties show some improvements in the subsurface. However, the low frequencies used still limit the updates to wavelengths in the order of hundreds of meters and therefore limit the resolution of the recovered layers. Further work in this problem will include higher frequencies in the inversion workflow, as well as better pre-conditioning of the gradients to address acquisition footprints and updates to the water column.

## ACKNOWLEDGEMENTS

I would like to thank Seabed Geosolutions for the use of this data set. I also thank Petrobras for supporting my PhD and SEP sponsors for the ongoing support.

## REFERENCES

Aki, K. and P. G. Richards, 1980, Quantitative seismology: Theory and methods, 1: I: WH Freeman and Co.

Alves, G., 2015, Adjoint formulation for the elastic wave equation: Stanford Exploration Project Report, **158**, 133–150.

Alves, G. and E. Biondi, 2017, Reciprocity in elastic multi-component data: Stanford Exploration Project Report, **168**, –.

Aster, R. C., B. Borchers, and C. H. Thurber, 2005, Parameter estimation and inverse problems: Elsevier Academic Press.

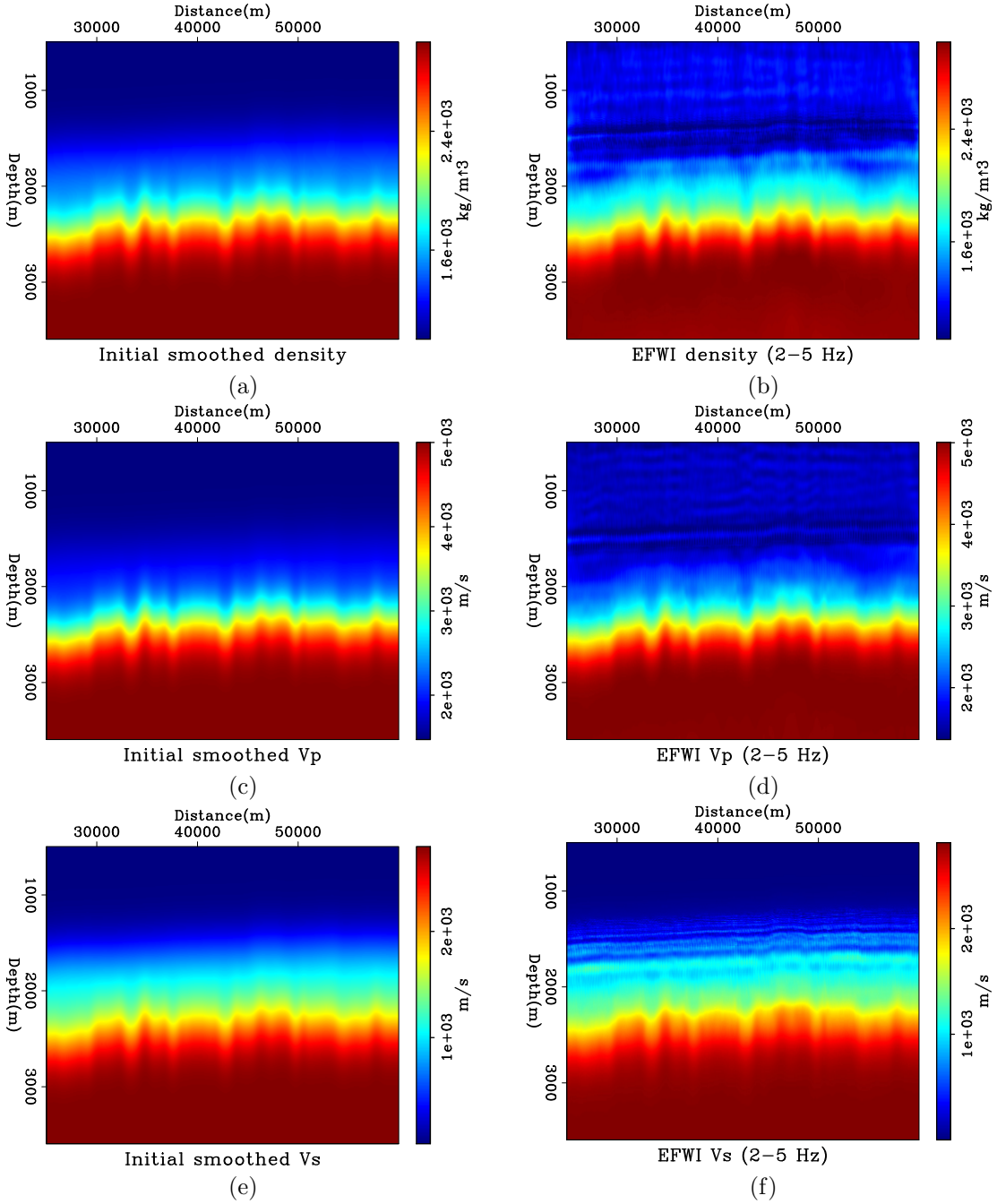


Figure 12: Comparison of (left) initial elastic properties and (right) after 2-5Hz EFWI. Inverted results have been smoothed horizontally to remove artifacts due to nodes geometry. [**CR**]

Biondi, E. and G. Barnier, 2017, A flexible out-of-core solver for linear/non-linear problems: Stanford Exploration Project Report, **168**, –.

Brekke, H., S. Dahlgren, B. Nyland, and C. Magnus, 1999, The prospectivity of the Vøring and Møre basins on the norwegian sea continental margin: Geological Society, London, Petroleum Geology Conference series, 261–274.

Claerbout, J. F. and S. Fomel, 2008, Image estimation by example: Geophysical soundings image construction: multidimensional autoregression.

Hager, W. W. and H. Zhang, 2006, A survey of nonlinear conjugate gradient methods: Pacific journal of Optimization, **2**, 35–58.

Levin, S. A. and J. P. Chang, 2015, Stable reorientation for the forties dataset: Stanford Exploration Project Report, **160**, 189–194.

Moronfoyer, A. T., S. Ronen, S. L. Klemperer, and G. Alves, 2016, Upper-crustal structure of the Møre margin, offshore-norway: 20016 AGU Fall Meeting, San Francisco, –.

Tarantola, A., 1987, Inverse problem theory: Methods for data fitting and model parameter estimation: Elsevier.